



# From coconut petiole residues to fluorescent carbon dots via a green hydrothermal method for Fe<sup>3+</sup> detection

Shiyu Gao · Xi Wang · Nan Xu · Hailan Lian · Li Xu · Wenqing Zhang · Changyan Xu 

Received: 24 September 2020 / Accepted: 14 December 2020 / Published online: 6 January 2021  
© The Author(s), under exclusive licence to Springer Nature B.V. part of Springer Nature 2021

**Abstract** Incinerating agricultural residues to recover energy is a popular method for reducing solid waste pollution and resource waste caused by the huge amount of coconut petiole residues. However, this process not only has the risk of secondary air pollution, but also the added value of comprehensive utilization is not high. In this paper, coconut petiole residues were used as eco-friendly and economical raw materials to synthesize carbon dots (CCDs) via a simple hydrothermal method. Furthermore, given the important reference significance of Fe<sup>3+</sup> concentration in assessing the quality of water environment and human body health, the obtained CCDs were utilized for Fe<sup>3+</sup> detection. The prepared spherical CCDs with an average diameter of 1.39 nm and a carbon skeleton dominated by benzene ring structure have surface

functional groups that endow them with good water solubility. The CCDs with a quantum yield of 1.39% emit strong blue fluorescence under ultraviolet radiation (365 nm), and show favorable fluorescence stability with excitation-dependent and concentration-dependent emission behaviors. Based on the synergetic effect of static and dynamic quenching, the CCDs exhibit favorable selectivity and detection sensitivity toward Fe<sup>3+</sup> with a linear range of 0.005 to 0.2 mM and a detection limit of 2.3 μM, and also show the feasibility of Fe<sup>3+</sup> detection in real water samples. This work is in favor of the high value-added conversion of coconut petiole residues. In addition, the development and use of bio-based CCDs as fluorescence sensors may be beneficial to monitoring and protecting public health and the environment.

S. Gao · X. Wang · N. Xu · H. Lian · L. Xu · C. Xu  
College of Materials Science and Engineering, Nanjing Forestry University, Nanjing 210037, China

S. Gao · N. Xu · H. Lian · L. Xu · C. Xu  
Jiangsu Co-Innovation Centre of Efficient Processing and Utilization of Forest Products, Nanjing Forestry University, Nanjing 210037, China

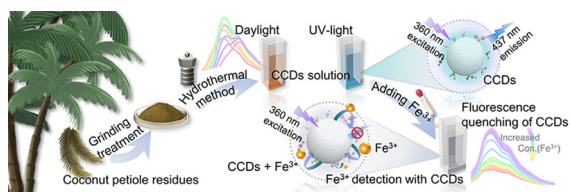
S. Gao · N. Xu · H. Lian (✉) · L. Xu · C. Xu (✉)  
Jiangsu Province Key Laboratory of Green Biomass-based Fuels and Chemicals, Nanjing Forestry University, Nanjing 210037, China  
e-mail: lianhailan@njfu.edu.cn

C. Xu  
e-mail: changyanxu1999@163.com

X. Wang  
Metrology and Testing Institute, Shanghai Institute of Quality Inspection and Technical Research, Shanghai 201114, China

W. Zhang  
Jiangsu Province Taizhou Efficient Processing Engineering Technology Research Center for Radiate Pine, Taizhou 214500, China

## Graphic abstract



**Keywords** Coconut petiole residues · Lignocellulose · Carbon dots · Hydrothermal method ·  $\text{Fe}^{3+}$  detection

## Introduction

Coconut (*Cocos nucifera* L.) is one of the three most economically important palm species in the world (Nayar 2017), and also one of the major crops providing livelihood security to millions in Asia and Pacific regions (Nampoothiri et al. 2018). Coconut trees provide a large quantity of eco-friendly economical raw materials during their growth and processing, such as inflorescence for sugar and vinegar, husks for coir mats, coconut shells for activated charcoal and ornaments, coconut leaves used for broomsticks, and coconut stems for furniture (Nayar 2017; Nampoothiri et al. 2018). Besides, coconut petioles, which have slight corrosion resistance, exist throughout the life cycle of coconut trees. Scattering such coconut petiole residues on roads or fields causes serious solid waste pollution, and their incineration also leads to air pollution. Although some studies have reported that it can be used as an alternative energy source (Nampoothiri et al. 2018) to isolate cellulose nanofibrils (Xu et al. 2015a) and fabricate cellulose nanofibril films (Zhao et al. 2015), the high value-added utilization of coconut petioles is far from enough compared with other coconut raw materials. Using underutilized coconut petiole residues to obtain high value-added products is not only beneficial to environmental protection, but also has economic benefits.

In theory, coconut petioles are appropriate for fabricating carbon nanomaterials, because they are rich in carbon and mainly composed of cellulose, hemicellulose and lignin (Xu et al. 2015a; Zhao et al. 2015; Bharath et al. 2019; Tejwan et al. 2020). Carbon dots (CCDs) are new members of the carbon

nanomaterials family, which were accidentally discovered when Xu et al. separated and purified single-walled carbon nanotubes in 2004 (Xu et al. 2004), and were subsequently named by Sun et al. (Sun et al. 2006). As an attractive type of zero-dimensional carbon nanomaterials with a size below 10 nm, CDs consist of an amorphous or crystalline carbon skeleton and a series of surface functional groups (Vandarkuzhali et al. 2017; Fan et al. 2020), which give them special fluorescence performance. Many studies show that CDs have great application potentials in fluorescence anti-counterfeiting (Yang et al. 2019a), bioimaging (Wang et al. 2019c; Atchudan et al. 2017, 2020a, b), detection analysis (Liu et al. 2019; Atchudan et al. 2018a), catalysis (Dhenadhayalan et al. 2020), and drug-delivery systems (Lin et al. 2020) due to their rich raw materials, easy synthesis routes, stable fluorescence performance, low cytotoxicity, and high aqueous solubility. CDs have been successfully derived from a variety of carbon sources, either man-made [e.g., carbon target (Sun et al. 2006) and citric acid (Zhu et al. 2013)] or natural products [e.g., aloe (Xu et al. 2015b), betel (Atchudan et al. 2019), grass (Sabet and Mahdavi 2019), rose-heart radish (Liu et al. 2017), peach (Atchudan et al. 2016), Indian gooseberry fruit (Atchudan et al. 2018c), and Jinhua bergamot (Yu et al. 2015)]. Compared with man-made carbon sources, eco-friendly natural products are cheaper, richer, greener, and easier to convert into high-value materials. In this study, we attempted to synthesize CDs from coconut petiole residues with a “bottom-up” method, hydrothermal method (Sun et al. 2020), which is more suitable for preparing natural products-based CDs because of such advantages as low-cost, eco-friendly, simple operation, sufficient reactions, and the relatively uniform particle size of prepared CDs (Zhang et al. 2018).

Due to industrialization and anthropogenic processes, excessive  $\text{Fe}^{3+}$  in the natural environment has become a kind of metal ion threatening the ecological environment and human health (Lin et al. 2019). Now, the concentration of  $\text{Fe}^{3+}$  is one of the important parameters for evaluating the quality of water environment and human body health. It is necessary to quantify  $\text{Fe}^{3+}$  concentration in water with favorable sensitivity and accuracy in the fields of biology and environment (Yan et al. 2016; Lv et al. 2020; Carvalho et al. 2019). However, compared with the use of CDs for  $\text{Fe}^{3+}$  detection, some of detection methods

summarized in previous reports suffer from time consuming and complication (Venkatesan et al. 2019; Wei et al. 2019).

Considering the fact that no open reports exist about coconut petiole residues-derived carbon dots (CCDs), we explored the possibility of fabricating carbon dots from coconut petiole residues via a hydrothermal method and using the obtained CCDs to detect  $\text{Fe}^{3+}$  in water in this work. Here, we used a hydrothermal method for preparing carbon dots that saved more time and energy than other studies reported (Ma et al. 2019; Huang et al. 2019). The morphology, structure, and optical properties of the CCDs were characterized, and the mechanism of  $\text{Fe}^{3+}$  detection using CCDs was also explored. This work provides a new approach for high value-added conversion of coconut petiole residues, which is in favor of environmental protection and agricultural waste utilization. Moreover, the development and use of bio-based CCDs obtained through large-scale, low-cost, and green production for  $\text{Fe}^{3+}$  detection may be beneficial to monitoring and protecting public health and environment.

## Materials and methods

### Materials

Coconut petiole residues powder with a size of 90 mesh was offered by Hainan Kunlun New Material Science and Technology Co., Ltd. (Hainan, China). After being oven-dried at 60 °C, the powder with a moisture content of 12% was sealed in a plastic bag for subsequent use.  $\text{H}_2\text{SO}_4$ ,  $\text{ZnCl}_2$ ,  $\text{KCl}$  and  $\text{NaCl}$  used in the experiment were purchased from Nanjing Chemical Reagent Co., Ltd. (Nanjing, China).  $\text{FeCl}_3$  and  $\text{CaCl}_2$  came from Sinopharm Chemical Reagents Co., Ltd. (Shanghai, China).  $\text{FeCl}_2 \cdot 4\text{H}_2\text{O}$ ,  $\text{CuCl}_2$ ,  $\text{NiCl}_2 \cdot 6\text{H}_2\text{O}$ , and Quinine sulfate (99.0%) were provided by Shanghai Rich Joint Chemical Reagent Co., Ltd. (Shanghai, China), Shanghai Xinbao Fine Chemical factory (Shanghai, China), Xilong Scientific Co., Ltd. (Shantou, China) and Shanghai Aladdin Biochemical Technology Co., Ltd. (Shanghai, China), respectively. All chemicals were analytical grade and used without further purification. Purified water was used throughout the experiment.

### Synthesis of CCDs

Carbon dots derived from coconut petiole residues were synthesized by a hydrothermal method (Sun et al. 2020) according to Scheme 1. Firstly, dry coconut petiole residues powder (1.0 g) was added into purified water (60 mL). After being stirred for 15 min at room temperature, the mixture was transferred into a polytetrafluoroethylene-equipped stainless-steel autoclave (100 mL) and heated at 180 °C for 10 h. After being cooled to room temperature naturally, the dark brown mixture taken from the autoclave was centrifuged (H-1650, Cence, China) at 9000 rpm for 10 min to remove the precipitation and retain the supernatant. Brown-yellow CCDs solution with a concentration of 2.33 mg/mL [calculated by a solution drying method (Xu et al. 2020) was obtained by filtering the centrifuged supernatant through a piece of filter membrane (0.22  $\mu\text{m}$ ). The solid CCDs for subsequent characterizations were prepared through vacuum freeze-drying (Alpha 1-2 LDplus, BMH, China).

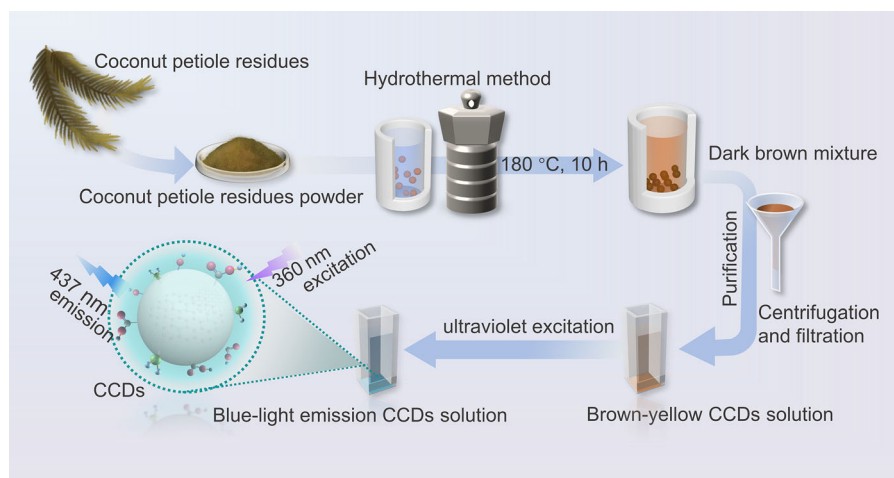
### Characterization of the CCDs

#### *Morphological characterization*

The morphology of the CCDs and their dispersion in water were analyzed by a high-resolution transmission electron microscope (HRTEM) (JEM-2100 UHR, JEOL, Japan) operated at an accelerating voltage of 200 kV. The sample for the test was obtained via drying an ultrathin carbon-coated copper grid coated with CCDs aqueous dispersion.

#### *Structural studies*

Fourier transform infrared spectroscopy (FTIR) spectra of the CCDs were recorded by an infrared spectrometer (VERTEX 80 V, Bruker, Germany). The mixture of solid CCDs powder and KBr (volume ratio 1:200) were ground and pressed into a transparent disk (Liu et al. 2017), and then scanned in the range of 4000–400  $\text{cm}^{-1}$ . The X-ray photoelectron spectroscopy (XPS) spectra of the prepared solid CCDs were carried out on an AXIS UltraDLD spectrometer (Shimadzu, Kyoto, Japan).



**Scheme 1** Synthesis process of CCDs by a hydrothermal method

### Optical properties studies

In this paper, the optical properties of the prepared CCDs were evaluated by ultraviolet–visible (UV–vis) absorption spectra, fluorescence (FL) spectra, fluorescence stability, and quantum yield (QY) analysis. The UV–vis absorption and FL spectra were recorded by a Lambda 950 UV–vis spectrophotometer (Perkin Elmer, USA) and a LS55 fluorescence spectrophotometer (Perkin Elmer, USA), respectively. In detail, the UV–vis absorption spectra were obtained with a scanning speed of 654.92 nm/min in the range of 200 to 800 nm, and the FL spectra were acquired with both excitation and emission slits of 5 nm, as well as a scanning speed of 300 nm/min. Fluorescence stability of the CCDs was also studied by exploring the effects of pH, ultraviolet irradiation duration, and NaCl concentration on the fluorescence intensity of CCDs. Specifically, the maximum fluorescence intensity of the CCDs under different acid–base (pH = 3–11) environmental media was recorded in sequence by using a fluorescence spectrophotometer (LS55, Perkin Elmer, USA) with the same test conditions as that of FL spectra investigation. Similarly, the maximum fluorescence intensity of the CCDs in the case of disparate ultraviolet irradiation duration (with the irradiation duration from 10 to 60 min) and diverse NaCl concentration (with the concentration of NaCl from 0 to 1.0 M) was also recorded by the above way. The QY of the CCDs was obtained by a sample reference method according to Eq. (1) (Zhang et al.

2016). Quinine sulfate (QY = 54%,  $\lambda_{\text{ex}} = 360$  nm) dissolved in  $\text{H}_2\text{SO}_4$  (0.1 M) was chosen as the standard reference to calculate the QY of the CCDs in purified water. All absorbance values were controlled under 0.1 with an excitation wavelength of 360 nm ( $\lambda_{\text{ex}} = 360$  nm) to avoid re-absorption, and all the FL spectra in QY determination were obtained by exciting at 360 nm with an excitation slit and an emission slit of 15 and 2.5 nm, respectively.

$$Q_{\text{sam}} = Q_{\text{ref}} \cdot (\text{Slop}_{\text{sam}}/\text{Slop}_{\text{ref}}) \cdot (N_{\text{sam}}/N_{\text{ref}})^2 \quad (1)$$

where  $Q_{\text{sam}}$  and  $Q_{\text{ref}}$  refer to the QY of the sample and the reference, respectively.  $\text{Slop}_{\text{sam}}$  and  $\text{Slop}_{\text{ref}}$  are the slopes from the plots of integrated fluorescence intensity versus absorbance of the sample and the reference, respectively.  $N_{\text{sam}}$  and  $N_{\text{ref}}$  represent the refractive indexes of the sample and the reference substance, respectively. In this work,  $N_{\text{sam}}$  and  $N_{\text{ref}}$  are the refractive index with 1.33 as the default for both CCDs and quinine sulfate.

### Fluorescence detection of $\text{Fe}^{3+}$ by CCDs

The detection of  $\text{Fe}^{3+}$  with the CCDs was performed by recording the fluorescence emission spectra. In detail, 1.0 mL of the prepared CCDs dispersion with a concentration of 0.2 mg/mL was first dispersed into 1.0 mL of phosphate-buffered saline (PBS, pH = 7), and then 1.0 mL of  $\text{Fe}^{3+}$  with different concentrations (0–1.0 M) was added into the mixture. The corresponding blank sample was also obtained by replacing

$\text{Fe}^{3+}$  with an equivalent amount of purified water. And then, the maximum fluorescence intensities excited at 360 nm of the above mixture samples and corresponding blank samples were respectively recorded as  $F$  and  $F_0$  value (LS55, Perkin Elmer, USA). The excitation and emission slits were 5 nm, and the scanning speed was 300 nm/min.

The limit of detection (LOD) was calculated according to Eq. (2) (Atchudan et al. 2018b).

$$\text{LOD} = 3\sigma/s \quad (2)$$

where  $\sigma$  refers to the standard deviation of the fluorescence intensities at the blank (the replica is 11), and  $s$  stands for the slope of the linear working curve.

Real water samples including tap and lake water samples were collected from our lab (Nanjing Forestry University, China) and Xuanwu lake (Nanjing, China), respectively. Firstly, the purified real samples were obtained by centrifuging the primary water samples at 9000 rpm for 15 min, followed by filtering with a piece of microporous membrane (0.22  $\mu\text{m}$ ) to remove suspended particles. Next, the CCDs solution (1.0 mL, 0.2 mg/mL), the purified real samples (1.0 mL), and  $\text{Fe}^{3+}$  (1.0 mL, with a concentration of 0, 30 and 40  $\mu\text{M}$ , separately) were mixed for detection and recovery calculation according to Eq. (3) (Liu et al. 2017).

$$\text{Recovery} = [(C_2 - C_1)/C_0] \times 100\% \quad (3)$$

where  $C_0$  represents the concentration of  $\text{Fe}^{3+}$  added into the purified real samples.  $C_1$  and  $C_2$  are the concentration of  $\text{Fe}^{3+}$  in purified real samples before and after adding  $\text{Fe}^{3+}$  with a known concentration, respectively.

## Results and discussion

### Structure and properties of CCDs

#### *Morphology and structure of CCDs*

The inset in the upper-right corner of Fig. 1a shows that the CCDs solution is light brown-yellow and bright blue under daylight and ultraviolet irradiation (UV, 365 nm), respectively. As also shown in Fig. 1a, the nanoparticles CCDs are spherical shape and well dispersed in aqueous solution without any

aggregation. Meanwhile, the average diameter of the prepared CCDs is calculated to be  $(1.39 \pm 0.22)$  nm (the inset in the lower-left corner of Fig. 1a), which is lower than 10 nm. The above results indicate that the CCDs with blue-emission fluorescence performance and good water solubility are successfully synthesized from coconut petiole residues through a simple hydrothermal method.

FTIR spectra are used to speculate the molecular structure and functional groups of the CCDs, as shown in Fig. 1b. In the FTIR spectrum of CCDs (the blue line, Fig. 1b), the strong and broad absorption peak appears at  $3429 \text{ cm}^{-1}$ , which is mainly due to the stretching vibration of O–H and N–H bonds (Ahn et al. 2019). The band at  $2972\text{--}2920 \text{ cm}^{-1}$  results from C–H stretching vibration (Sabet and Mahdavi 2019). The weak peaks at  $1749 \text{ cm}^{-1}$  and  $1157 \text{ cm}^{-1}$  are caused by the presence of C=O and C–O–C bonds, respectively (Wei et al. 2019). The strong band at  $1612\text{--}1517 \text{ cm}^{-1}$  is related to the stretching vibration of C=C, indicating that there exist  $sp^2$  structures in the CCDs (Huang et al. 2019). The absorption peak at  $1400 \text{ cm}^{-1}$  is attributed to the C–N stretching vibration, and the sharp peak located at  $1055 \text{ cm}^{-1}$  corresponds to C–O bonds (Ahn et al. 2019). To further explore the structural composition of the CCDs, the FTIR spectrum of their carbon source (the yellow line, Fig. 1b), coconut petiole residues, was also carried out. The wavenumber and corresponding ascription in the FTIR spectra of coconut petiole residues and CCDs were summarized in Table 1. There are similarities in general and subtle differences in details between the two FTIR spectra. Their resemblances, analogical absorption peaks caused by C–H ( $2972\text{--}2848 \text{ cm}^{-1}$ ), C=O ( $1749\text{--}1735 \text{ cm}^{-1}$ ), C=C ( $1631\text{--}1612 \text{ cm}^{-1}$  and  $1517\text{--}1515 \text{ cm}^{-1}$ ), C–N ( $1400 \text{ cm}^{-1}$ ), C–O–C ( $1243\text{--}1155 \text{ cm}^{-1}$ ), as well as C–O ( $1064\text{--}1055 \text{ cm}^{-1}$ ) bonds, suggest that there also exist chemical structures similar to their carbon source in CCDs (Zhao et al. 2015). However, compared with the FTIR spectrum of coconut petiole residues, the intensities of absorption peaks attributed to C=C ( $1612 \text{ cm}^{-1}$ ), C–N ( $1400 \text{ cm}^{-1}$ ), and C–O ( $1055 \text{ cm}^{-1}$ ) bands in that of CCDs are stronger. Furthermore, obvious peaks belong to stretching vibration ( $2972 \text{ cm}^{-1}$ ) and bending vibration ( $897$  and  $781 \text{ cm}^{-1}$ ) of C–H bond merely appear in the FTIR spectrum of CCDs. It can be explained by the fact that coconut petiole residues powder generally

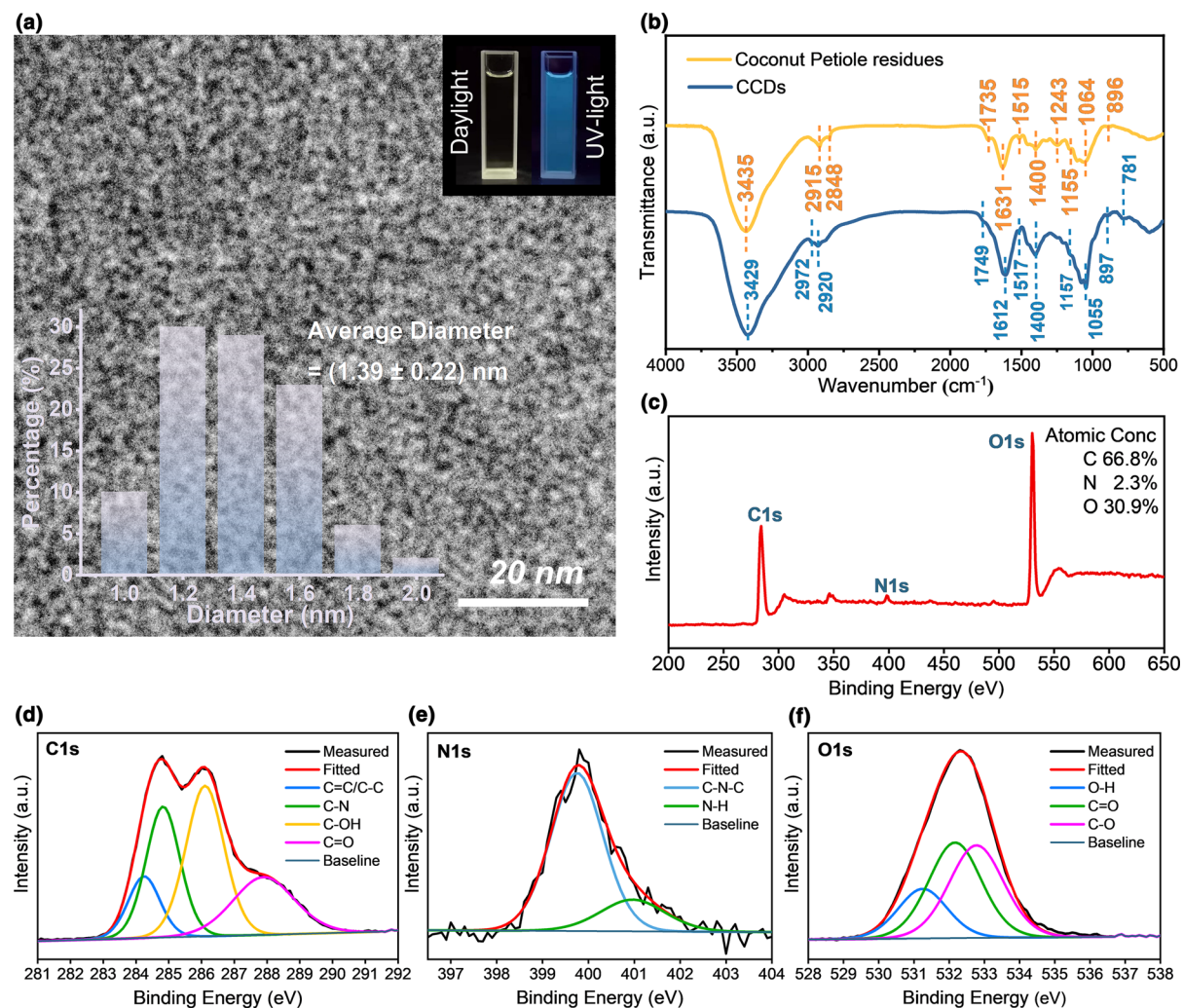


**Fig. 1** **a** Morphology graph of the CCDs obtained by HRTEM, in which the inset in the upper-right corner are optical images under daylight (left) and UV light (right), respectively, and the inset in the lower-left corner is the particle size distribution of

CCDs. **b** FTIR spectra of CCDs and their corresponding carbon source (coconut petiole residues). XPS full-scan spectrum (**c**) and their corresponding high-resolution spectrum of C1s (**d**), N1s (**e**), and O1s (**f**) of CCDs

undergoes several changing stages during hydrothermal treatment, including dehydration, condensation, polymerization, and carbonization or aromatization to form numerous carbon skeleton and surface functional groups of CCDs (Tejwan et al. 2020; Wang et al. 2019c). More specifically, the hydrothermal treatment allows hot compressed water to access the inner structure of coconut petiole residues, leading the crystalline-to-amorphous transformation of cellulose and then to fast reaction rates to form oligomers (Paksung et al. 2020). Hemicellulose, a light component, can decompose at 160 °C (Sulaiman et al. 2016). In addition, lignin may undergo wet oxidation at

elevated temperature (100–320 °C) and pressure (0.5–20 MPa). In the wet oxidation of lignin, the aromatic aldehydes can be produced by cleavage of ether bond and appropriate oxidation of  $\alpha$  C in phenylpropane (Kang et al. 2013). Above analyses show that the CCDs contain  $sp^2$  structures similar to the benzene ring, and have lots of –OH as well as –COOH, and a small number of –NH<sub>2</sub> groups on the surface.

XPS spectra are introduced to further explore the elemental composition and chemical state of the CCDs surface, as shown in Fig. 1c. Three signal peaks at 284.8, 399.8, and 532.3 eV in the XPS full-scan

**Table 1** Wavenumber and the corresponding ascription in the FTIR spectra of coconut petiole residues and CCDs

Wavenumber (cm <sup>-1</sup> )	Attribution in the coconut petioles sample		Attribution in the prepared CCDs sample	
	Functional groups	Composition (Xu et al. 2015a; Zhao et al. 2020)	Functional groups	Location
3435–3429	O–H/N–H	Cellulose, hemicellulose, lignin	–OH/–NH	S* (Dhenadhayalan et al. 2020)
2972–2848	H–C–H	Cellulose, hemicellulose	–CH	–
1749–1735	C=O	Hemicellulose	–COOH	S (Wang et al. 2019b)
1631–1612	C=C	Hemicellulose	C=C	C (Zhao et al. 2020)
1517–1515	C=C	Lignin		
1400	C–N	Lignin	–C–NH <sub>2</sub>	S (Sabet and Mahdavi 2019)
1243–1155	C–O–C	Cellulose, lignin	C–O–C	–
1064–1055	C–O	Cellulose, lignin	–C–OH	S (Sabet and Mahdavi 2019)
900–700	C–H	Cellulose, lignin	–CH	–

\* “S” and “C” represent “Surface functional group” and “Carbon skeleton”, respectively

spectrum of CCDs, are ascribed to C, N, and O elements with the relative atomic ratios as 66.8, 2.3, and 30.9%, respectively (Wang et al. 2019c). By peak fitting, the high-resolution XPS spectrum (Fig. 1d) of C1s displays four peaks at 284.2, 284.8, 286.1, and 287.9 eV, which can be assigned to C=C/C–C, C–N, C–OH, and C=O, respectively (Atchudan et al. 2018b; Wang et al. 2019b). Similarly, the high-resolution spectrum of N1s (Fig. 1e) contains C–N–C (399.7 eV) and N–H (401.0 eV) (Zhang et al. 2019a). Additionally, the high-resolution spectrum of O1s presents three peaks at 531.3, 532.2, and 532.8 eV (Fig. 1f), corresponding to the binding energies of O–H, C=O, and C–O, respectively (Zhang et al. 2019a; Yang et al. 2019b). The founding in the XPS spectra reveals that the CCDs are carbon-rich with nitrogen and oxygen, which confirms the result of the above FTIR analysis.

In brief, both FTIR and XPS investigation show that coconut petiole residues are decomposed and carbonized to form CCDs with a carbon skeleton dominated by benzene ring structure and surface functional groups such as –COOH, –OH, –NH<sub>2</sub> by hydrothermal carbonization. The CCDs possess good water solubility because of these hydrophilic groups, which is consistent with the results of TEM analysis. Besides, as summarized in the previous report, the selectivity of CDs towards Fe<sup>3+</sup> is related to the interaction between Fe<sup>3+</sup> and carboxyl, hydroxyl or

amino groups on the surface of CDs (Wang et al. 2019b). Therefore, it is expected that the CCDs should have potential applications in Fe<sup>3+</sup> detection in water.

#### Optical properties of CCDs

The QY of the prepared CCDs is determined by the sample reference method. Figure 2a shows that the *Slop<sub>sam</sub>* and *Slop<sub>ref</sub>* are 20,122.12 and 780,792.98, respectively. According to Eq. (1), the QY of CCDs without any dopant is 1.39%.

In Fig. 2b, the central position of the fluorescence emission peak of the CCDs gradually red-shifts from 437 (corresponding to blue light) to 493 nm (corresponding to cyan light) when the excitation wavelength varies from 320 to 400 nm. It indicates that the fluorescence emission performance of CCDs is related to excitation wavelength, which is similar to some previous reports (Ahn et al. 2019; Wang et al. 2019b). Generally, the excitation-dependent emission behaviors of CDs may attribute to two commonly accepted fluorescence mechanism, size-dependent quantum confinement effect and surface state emission effect (Tejwan et al. 2020; Wang et al. 2019b). As shown in the lower-left corner inset of Fig. 1a, the particle size of the CCDs with a small distribution range of 0.93 to 2.01 nm is homogeneous (Sun et al. 2020), demonstrating that this excitation-dependent emission

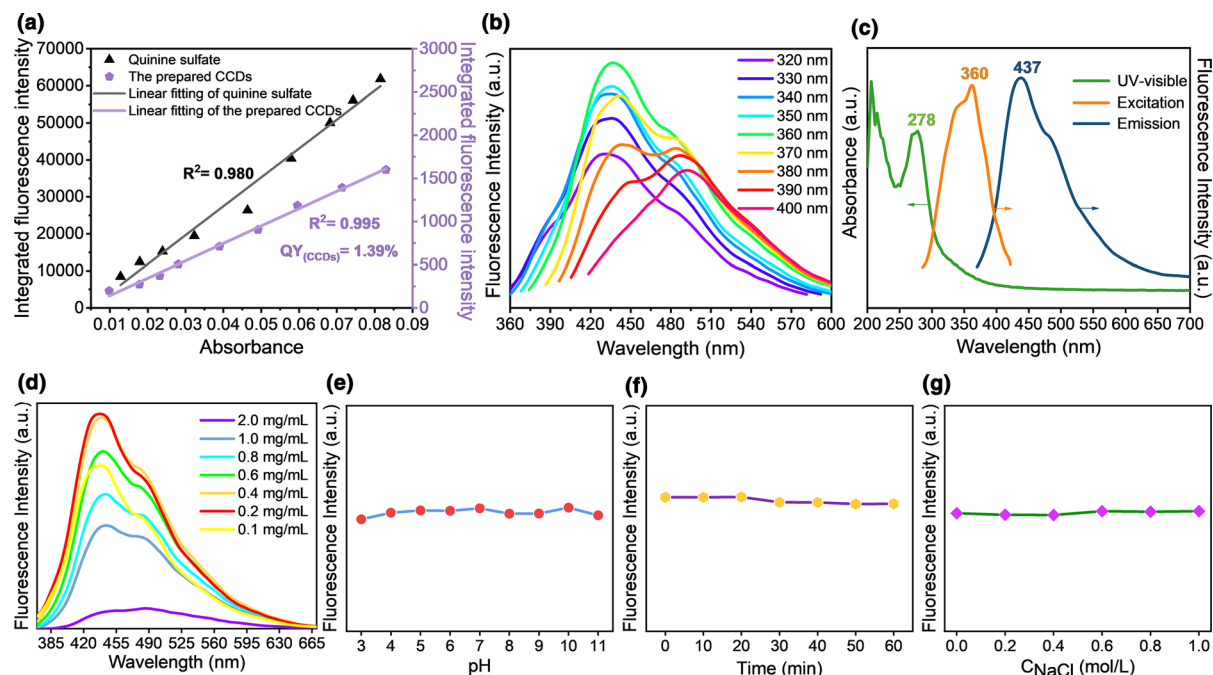


**Fig. 2** a The QY determination of CCDs. FL emission spectra excited at the wavelength from 320 to 400 nm (b), UV–vis absorption, optimal FL excitation and emission spectra (c), FL emission spectra with the concentration from 2.0 to 0.1 mg/mL

phenomenon is not mainly due to size-dependent quantum confinement effect. Moreover, the surface functional groups of CCDs (such as  $-\text{COOH}$ ,  $-\text{OH}$ , and  $-\text{NH}_2$ ) may serve as capture centers for excitons to form multiple emission sites or defect sites, giving rise to surface-state-related fluorescence of the CCDs (Ding et al. 2016). Therefore, the excitation-dependent behavior of the CCDs is mainly affected by the distribution of different surface states and particle size, and the surface state is the dominant factor. It's worth noting that the fluorescence intensity of CCDs exhibits a maximum value excited at 360 nm, and the corresponding emission wavelength is 437 nm. So, we choose 360 nm as excitation wavelength in the subsequent CCDs application experiments for detecting  $\text{Fe}^{3+}$  in water.

Figure 2c shows the UV–vis absorption, optimal FL excitation and emission spectra of the prepared CCDs. The CCDs possess optical absorption capacity in the ultraviolet region, which is consistent with other literature reports (green line) (Ahn et al. 2019; Jia et al. 2019). Their absorption peak mainly exists in the ultraviolet region with a wavelength of 245 to 290 nm,

excited at 360 nm (d), and the effect of pH (e), ultraviolet irradiation duration (f), and NaCl concentration (g) on FL intensity of CCDs

and the maximum peak corresponds to 278 nm, which is assigned to  $\pi-\pi^*$  electronic transitions of  $\text{C}=\text{C}$  bond (Jia et al. 2019; Yang et al. 2020a). The orange and blue lines respectively correspond to the optimal FL excitation (360 nm) and emission (437 nm) spectra of the CCDs, which also confirms that the CCDs emit blue fluorescence under ultraviolet irradiation.

In order to determine the most appropriate CCDs concentration suitable for the subsequent application, the effect of CCDs concentration on the fluorescence intensity was also investigated, and the result was shown in Fig. 2d. As the concentration of CCDs decreased from 2.0 to 0.2 mg/mL, the corresponding fluorescence intensities demonstrate a gradually increasing trend; however, further decreasing the concentration from 0.2 to 0.1 mg/mL leads to a reduction in fluorescence intensity. In a word, the maximum value appears in the CCDs concentration of 0.2 mg/mL under the excitation wavelength of 360 nm. Such a concentration-dependent emission phenomenon indicates that too high or too low concentration of CCDs is not suitable for satisfactory optical properties. In the case of high concentration of



CCDs, hydrogen bonds are easily formed between CCDs molecules due to their surface structure, forming non-fluorescent emission associations molecular, and then leading to fluorescence self-quenching effect. At the same time, the decrease in CCDs content in low concentration will also weaken the fluorescence emission intensity. In the subsequent CCDs application experiments for detecting  $\text{Fe}^{3+}$  in water, the concentration of CCDs is selected as 0.2 mg/mL.

As revealed in Fig. 2e–g, the fluorescence emission intensities of the prepared CCDs hardly change with the change of acid–base environment, ultraviolet irradiation duration, and the concentration of NaCl. In other words, the CCDs demonstrate favorable stability to tolerate the changes in pH, photobleaching, and high NaCl concentration, which is needed for  $\text{Fe}^{3+}$  detection in complex circumstances.

Based on the optical properties and structural composition, it can be concluded that the fluorescence emission mechanism of CCDs is jointly established by the surface state effect, the carbon skeleton structure, and the size effect, in which the surface state is the dominant factor.

Application of the prepared CCDs in detecting  $\text{Fe}^{3+}$

#### *Mechanism of $\text{Fe}^{3+}$ fluorescence detection by the CCDs*

The fluorescence intensities of the CCDs with and without a certain concentration of  $\text{Fe}^{3+}$  (1.0 M) were measured. As revealed in Fig. 3a, compared with the  $\text{Fe}^{3+}$ -free CCDs, the CCDs containing  $\text{Fe}^{3+}$  shows a significantly weaker fluorescence intensity. Here, the quenching mechanism was investigated for understanding the interaction between  $\text{Fe}^{3+}$  and CCDs. Usually, the fluorescence quenching mechanism includes static quenching and dynamic quenching (Yang et al. 2020b). And more specifically, static quenching refers to the formation of complexes by combining ground-state molecules of CCDs with  $\text{Fe}^{3+}$ , while dynamic quenching means the collision of excited-state CCDs with  $\text{Fe}^{3+}$  (Yu et al. 2015). Static quenching will generate new ground-state substances, causing the change of absorption spectrum of CCDs, but does not affect the fluorescence lifetime of CCDs, while dynamic quenching is the opposite. To further explore the quenching mechanism of the CCDs

with  $\text{Fe}^{3+}$ , UV–vis absorption spectra and fluorescence decay curves were also performed (Fig. 3b). Compared with the spectrum of CCDs (blue dotted line), the absorption peak of CCDs +  $\text{Fe}^{3+}$  (red line) shows a blue shift, indicating the formation of new ground-state substances (Wang et al. 2019a). Moreover, the experimental curve (the absorption spectrum of CCDs +  $\text{Fe}^{3+}$ , red line) does not coincide with the theoretical one (the physical addition of the spectra of CCDs and  $\text{Fe}^{3+}$ , green line), demonstrating the formation of stable CCDs/ $\text{Fe}^{3+}$  complexes and also supporting the static quenching explanation in the quenching process (Gao et al. 2018). The above results provide evidence for the static quenching mechanism existing in the interaction between  $\text{Fe}^{3+}$  and CCDs. Nevertheless, in terms of the average fluorescence lifetime, they are 3.09 ns and 1.05 ns (Fig. 3c) for CCDs and CCDs +  $\text{Fe}^{3+}$ , respectively. Such a decrease in fluorescence lifetime indicates that the phenomenon of fluorescence quenching is also the result of electron transfer in dynamic quenching between  $\text{Fe}^{3+}$  and the excited state of CCDs (Carvalho et al. 2019). In conclusion, the synergetic effect of both static and dynamic quenching between CCDs and  $\text{Fe}^{3+}$  is responsible for the fluorescence quenching of CCDs with  $\text{Fe}^{3+}$ . The possible mechanism diagram of  $\text{Fe}^{3+}$  detection with CCDs is shown in Fig. 3d.

#### *Fluorescence analysis of detecting $\text{Fe}^{3+}$*

Based on the synergetic effect of static and dynamic quenching between  $\text{Fe}^{3+}$  and CCDs, Fig. 4 reveals the different degree of fluorescence quenching of CCDs by  $\text{Fe}^{3+}$  (Fig. 4a), the quenching efficiency ( $F_0/F$ ) (Fig. 4b), and the corresponding linear fitting curves for  $\text{Fe}^{3+}$  detection (Fig. 4c–d). As illustrated in Fig. 4a, the fluorescence intensities of CCDs excited at 360 nm gradually decrease with increasing the  $\text{Fe}^{3+}$  concentration from 0 to 1.0 mM, demonstrating that the prepared CCDs are sensitive to the concentration of  $\text{Fe}^{3+}$  and suitable for quantitative determination. The relationship between  $F_0/F$  and the concentration of  $\text{Fe}^{3+}$  (Fig. 4b) displays a good linear correlation within the concentration range of 0.005 to 0.2 mM and 0.2 to 1.0 mM, respectively. Hence, two working curves for quantitative  $\text{Fe}^{3+}$  detection in different operating conditions were obtained. One is  $y = 4.9374x + 1.02473$  ( $R^2 = 0.994$ ) with the measuring range of 0.005 to 0.2 mM (Fig. 4c), and the

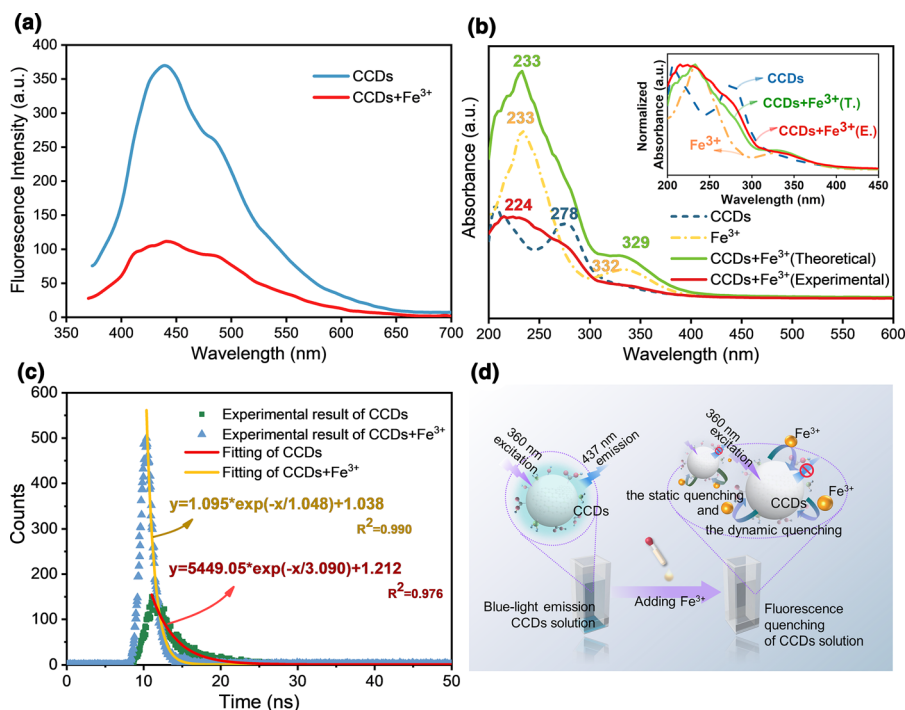


**Fig. 3** **a** The FL spectra of CCDs with and without a certain concentration of Fe<sup>3+</sup>. **b** UV–vis absorption spectra of CCDs, Fe<sup>3+</sup>, as well as CCDs/Fe<sup>3+</sup> in the experimental and theoretical (inset: normalized UV–vis absorption spectra). **c** The

fluorescence decay curves of CCDs in the absence and presence of Fe<sup>3+</sup>. **d** The possible mechanism schematic diagram of Fe<sup>3+</sup> detection with CCDs

other is  $y = 1.65344x + 1.72306$  ( $R^2 = 0.997$ ) over the measuring range of 0.2–1.0 mM (Fig. 4d). And the LOD was calculated to be 2.3  $\mu\text{M}$  according to Eq. (2). As summarized in Table 2, compared with some previous reports, the LOD of our CCDs for Fe<sup>3+</sup> detection is smaller, indicating that the CCDs derived from coconut petiole residues also possess a higher sensitivity in Fe<sup>3+</sup> detection. According to the “Secondary Drinking Water Standards: Guidance for Nuisance Chemicals” (Sarih et al. 2020) issued by Environmental Protection Agency (EPA) and the “Standards for drinking water quality (GB5749-2006)” currently implemented in China, the concentration of iron in drinking water should be less than 0.3 mg/L ( $\sim 5.36 \mu\text{M}$ ). Therefore, the CCDs for Fe<sup>3+</sup> determination with a detection limit of 2.3  $\mu\text{M}$  may be useful for detecting Fe<sup>3+</sup> in real samples of biological and environmental systems (Zhang et al. 2020).

To investigate the selective recognition capability of the CCDs towards Fe<sup>3+</sup> in environmental conditions, various common metal ions (Fe<sup>2+</sup>, Ca<sup>2+</sup>, Cu<sup>2+</sup>,

Ni<sup>2+</sup>, Zn<sup>2+</sup>, K<sup>+</sup>, and Na<sup>+</sup>) were selected as interference ions for control experiments. In Fig. 5a, c, compared with the blank sample (the fluorescence intensity of CCDs without metal ions), the fluorescence intensity of CCDs decreases and increases obviously after adding Fe<sup>3+</sup> and Fe<sup>2+</sup>, respectively, while introducing other ions into CCDs does not cause significant changes. In general, excited-state molecules have stronger redox properties than ground-state ones. The excited-state CCDs reveal reducibility when Fe<sup>3+</sup> exhibits oxidation performance. The existence of electron transfer between the excited-state CCDs and Fe<sup>3+</sup> causes a decrease in the fluorescence lifetime of CCDs, displaying the fluorescence quenching phenomenon. Similarly, the electron transfer between Fe<sup>2+</sup> with reducibility and the excited-state CCDs with oxidation properties leads to an increase in the fluorescence intensity of CCDs. This also confirms that there exists dynamic quenching between Fe<sup>3+</sup> and the excited-state CCDs with oxidation–reduction ability. In addition, the CCDs still shows well recognizability toward Fe<sup>3+</sup> in the case of other metal

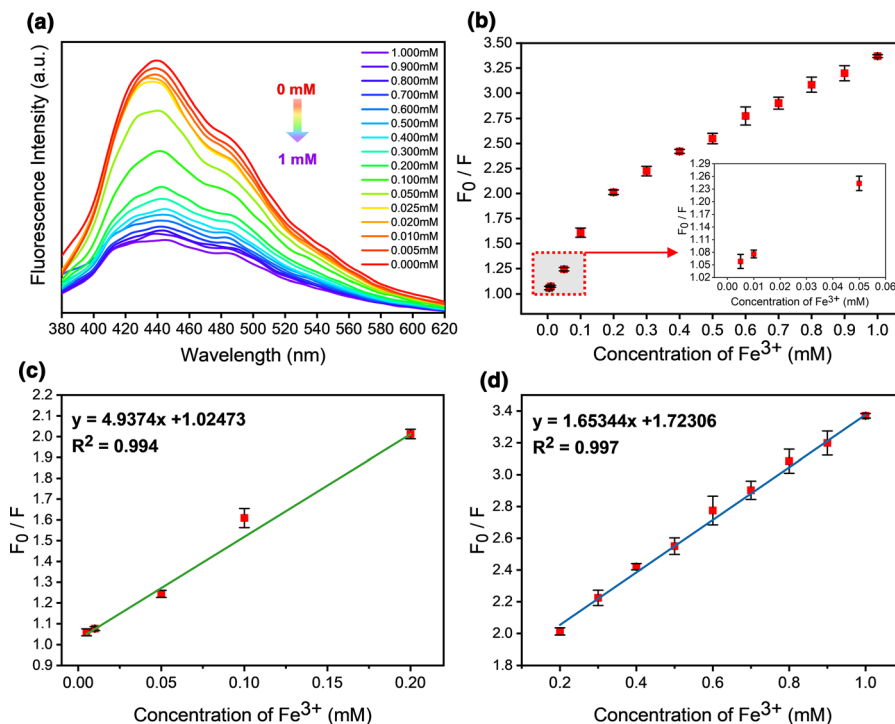


**Fig. 4** **a** FL spectra of the CCDs with different concentrations of  $\text{Fe}^{3+}$ . **b** The relationship between  $F_0/F$  and concentration of  $\text{Fe}^{3+}$ . Two working curves of CCDs for  $\text{Fe}^{3+}$  detection based on

linear fitting with the concentration of  $\text{Fe}^{3+}$  in 0.005–0.2 mM (**c**) and 0.2–1.0 mM (**d**). *Note* Error bars indicate the standard deviation of 3 replicates from each testing specimens

**Table 2** Comparison of different fluorescent CDs for  $\text{Fe}^{3+}$  detection

Carbon source	Linear range ( $\mu\text{M}$ )	LOD ( $\mu\text{M}$ )	References
Food waste	0–500	32.00	Ahn et al. (2019)
Blueberry	12.5–100	9.97	Aslandaş et al. (2015)
Black sesame	50–1500	2.78	Zhang et al. (2019b)
Roasted-chickpea	9.38–37.50	2.74	Başoğlu et al. (2020)
Coconut petioles	5–200	2.30	Present work

ions interference. As shown in Fig. 5b, d, the fluorescence intensity of the mixture with  $\text{Fe}^{3+}$  (CCDs +  $\text{M}^{n+}$  +  $\text{Fe}^{3+}$ , yellow columns,  $\text{M}^{n+}$ :  $\text{Fe}^{2+}$ ,  $\text{Ca}^{2+}$ ,  $\text{Cu}^{2+}$ ,  $\text{Ni}^{2+}$ ,  $\text{Zn}^{2+}$ ,  $\text{K}^+$ , or  $\text{Na}^+$ ) is obviously lower than that of the mixture without  $\text{Fe}^{3+}$  (CCDs +  $\text{M}^{n+}$ , blue columns), which indicates that the CCDs are selective to  $\text{Fe}^{3+}$  in the mixture. Theoretically,  $\text{Fe}^{3+}$  has a stronger binding affinity and faster chelating kinetics with amino and carboxylic groups on the CCDs surfaces in comparison with the other metal ions (Yu et al. 2015), which causes fluorescence quenching of CCDs, and also provides a basis for static quenching. In summary, the prepared CCDs are able to eliminate the interference

of other metal ions such as  $\text{Fe}^{2+}$ ,  $\text{Ca}^{2+}$ ,  $\text{Cu}^{2+}$ ,  $\text{Ni}^{2+}$ ,  $\text{Zn}^{2+}$ ,  $\text{K}^+$ , and  $\text{Na}^+$  in the complex environment, and realize the selective recognition of  $\text{Fe}^{3+}$ . Thus, a conclusion is made that the CCDs prepared from coconut petiole residues have the potential to develop efficient fluorescence sensors for  $\text{Fe}^{3+}$  detection.

#### *Fe<sup>3+</sup> detection in real samples*

In order to verify the practicability of CCDs in detecting  $\text{Fe}^{3+}$ , the CCDs have been extended to  $\text{Fe}^{3+}$  determination in real water samples covering tap and lake water. The results are shown in Table 3. The recoveries of all samples are between 99.00 and

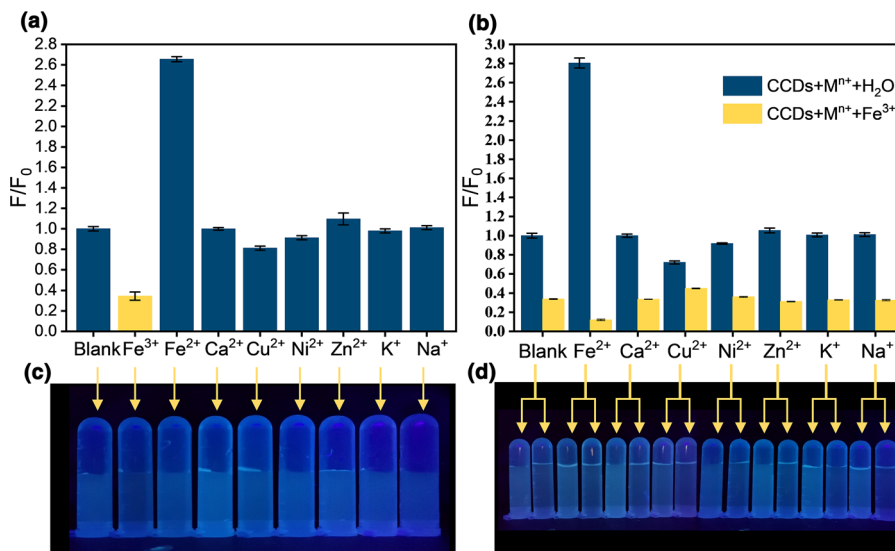


**Fig. 5** a Fluorescence response between CCDs and the selected interference ions (Fe<sup>3+</sup>, Fe<sup>2+</sup>, Ca<sup>2+</sup>, Cu<sup>2+</sup>, Ni<sup>2+</sup>, Zn<sup>2+</sup>, K<sup>+</sup> and Na<sup>+</sup>). b Fluorescence intensities of CCDs containing metal ions

before and after adding Fe<sup>3+</sup>, and the corresponding experimental pictures (c–d)

**Table 3** Analysis of Fe<sup>3+</sup> detection using the prepared CCDs in real samples (n = 3)

Sample	Added (μM)	Found (μM)	Recovery (%)	RSD (%)
Tap water	30.00	28 ± 0.72	112.00	2.10
	40.00	40 ± 5.03	111.00	11.30
Lake water	30.00	26 ± 1.11	104.00	3.60
	40.00	35 ± 5.50	99.00	13.80

112.00% according to Eq. (3), and the relative standard deviations (RSDs) are from 2.10 to 13.80%. The above results demonstrate that it is feasible to detect Fe<sup>3+</sup> in real environmental water using the CCDs. All advantages of this research, including abundant and renewable coconut resources, eco-friendly synthesis process of CCDs, simple Fe<sup>3+</sup> detection process, as well as reliable detection results, confirm the potential and feasibility of further development and application of CCDs for Fe<sup>3+</sup> detection.

## Conclusion

In summary, as a green carbon source, the underutilized coconut petiole residues were decomposed, carbonized, and successfully converted into the high value-added CCDs via a simple hydrothermal method. The obtained spherical CCDs with an average diameter of 1.39 nm and a carbon skeleton dominated by

the benzene ring structure have such surface functional groups as –COOH, –OH, –NH<sub>2</sub> that give them good water solubility. Due to the fluorescence mechanism dominated by surface state, the CCDs with a QY of 1.39% show the excitation-dependent and concentration-dependent emission behaviors, and exhibit blue fluorescence under ultraviolet radiation (365 nm). Besides, the CCDs demonstrate favorable fluorescence stability to tolerate the changes in pH, photobleaching, and high NaCl concentration. Based on the synergetic effect of static and dynamic quenching, the CCDs exhibit favorable selectivity and sensitivity toward Fe<sup>3+</sup> with a linear range from 0.005 to 0.2 mM and a LOD of 2.3 μM, and also display the practicality of Fe<sup>3+</sup> detection in real water samples. The present work provides a new way for high value-added conversion of coconut petiole residues, which is in favor of environmental protection and agricultural waste utilization. In addition, the development and use of bio-based CCDs obtained

through large-scale, low-cost, and green production for Fe<sup>3+</sup> detection may be beneficial to monitoring and protecting public health and environment in complex circumstances. Moreover, fluorescent sensors developed on CCDs are also expected to be used for other ion or molecular detection.

**Acknowledgments** The authors would like to thank the First-Class Discipline Construction, the International Innovation Highland of Forest Product Chemistry, the Taizhou Efficient Processing Engineering Technology Research Center for Radiata Pine, and the Advanced Analysis and Testing Center of Nanjing Forestry University for their support.

**Funding** This work was supported by the National Natural Science Foundation of China (No. 32071703).

#### Compliance with ethical standards

**Conflict of interest** The authors declare that they have no conflict of interest.

**Research involving human participants and/or animals** This research did not involve human participants and animals.

**Informed consent** The informed consent was not required for this research that did not involve human participants.

**Statement on welfare of animals** The statement on welfare of animals was not required for this research that did not involve animals.

## References

- Ahn J, Song Y, Kwon JE et al (2019) Food waste-driven N-doped carbon dots: applications for Fe<sup>3+</sup> sensing and cell imaging. *Mater Sci Eng, C* 102:106–112. <https://doi.org/10.1016/j.msec.2019.04.019>
- Aslandaş AM, Balci N, Arik M et al (2015) Liquid nitrogen-assisted synthesis of fluorescent carbon dots from Blueberry and their performance in Fe<sup>3+</sup> detection. *Appl Surf Sci* 356:747–752. <https://doi.org/10.1016/j.apsusc.2015.08.147>
- Atchudan R, Edison TNJI, Lee YR (2016) Nitrogen-doped carbon dots originating from unripe peach for fluorescent bioimaging and electrocatalytic oxygen reduction reaction. *J Colloid Interface Sci* 482:8–18. <https://doi.org/10.1016/j.jcis.2016.07.058>
- Atchudan R, Edison TNJI, Chakradhar D et al (2017) Facile green synthesis of nitrogen-doped carbon dots using *Chionanthus retusus* fruit extract and investigation of their suitability for metal ion sensing and biological applications. *Sensors Actuators, B Chem* 246:497–509. <https://doi.org/10.1016/j.snb.2017.02.119>
- Atchudan R, Edison TNJI, Aseer KR et al (2018a) Hydrothermal conversion of *Magnolia liliiflora* into nitrogen-doped carbon dots as an effective turn-off fluorescence sensing, multi-colour cell imaging and fluorescent ink. *Colloids Surfaces B Biointerfaces* 169:321–328. <https://doi.org/10.1016/j.colsurfb.2018.05.032>
- Atchudan R, Edison TNJI, Aseer KR et al (2018b) Highly fluorescent nitrogen-doped carbon dots derived from *Phyllanthus acidus* utilized as a fluorescent probe for label-free selective detection of Fe<sup>3+</sup> ions, live cell imaging and fluorescent ink. *Biosens Bioelectron* 99:303–311. <https://doi.org/10.1016/j.bios.2017.07.076>
- Atchudan R, Edison TNJI, Perumal S, Lee YR (2018c) Indian gooseberry-derived tunable fluorescent carbon dots as a promise for in vitro/in vivo multicolor bioimaging and fluorescent ink. *ACS Omega* 3:17590–17601. <https://doi.org/10.1021/acsomega.8b02463>
- Atchudan R, Edison TNJI, Perumal S et al (2019) Betel-derived nitrogen-doped multicolor carbon dots for environmental and biological applications. *J Mol Liq* 296:111817. <https://doi.org/10.1016/j.molliq.2019.111817>
- Atchudan R, Edison TNJI, Perumal S et al (2020a) Hydrophilic nitrogen-doped carbon dots from biowaste using dwarf banana peel for environmental and biological applications. *Fuel* 275:117821. <https://doi.org/10.1016/j.fuel.2020.117821>
- Atchudan R, Edison TNJI, Perumal S et al (2020b) Eco-friendly synthesis of tunable fluorescent carbon nanodots from *Malus floribunda* for sensors and multicolor bioimaging. *J Photochem Photobiol A Chem* 390:112336. <https://doi.org/10.1016/j.jphotochem.2019.112336>
- Başoğlu A, Ocak Ü, Gümriükçüoğlu A (2020) Synthesis of microwave-assisted fluorescence carbon quantum dots using roasted-chickpeas and its applications for sensitive and selective detection of Fe<sup>3+</sup> ions. *J Fluoresc* 30:515–526. <https://doi.org/10.1007/s10895-019-02428-7>
- Bharath KN, Sanjay MR, Jawaid M et al (2019) Effect of stacking sequence on properties of coconut leaf sheath/jute/E-glass reinforced phenol formaldehyde hybrid composites. *J Ind Text* 49:3–32. <https://doi.org/10.1177/1528083718769926>
- Carvalho J, Santos LR, Germino JC et al (2019) Hydrothermal synthesis to water-stable luminescent carbon dots from acerola fruit for photoluminescent composites preparation and its application as sensors. *Mater Res* 22(3):e20180920. <https://doi.org/10.1590/1980-5373-MR-2018-0920>
- Dhenadhayalan N, Lin KC, Saleh TA (2020) Recent advances in functionalized carbon dots toward the design of efficient materials for sensing and catalysis applications. *Small* 16:1905767. <https://doi.org/10.1002/sml.201905767>
- Ding H, Yu SB, Wei JS, Xiong HM (2016) Full-color light-emitting carbon dots with a surface-state-controlled luminescence mechanism. *ACS Nano* 10:484–491. <https://doi.org/10.1021/acsnano.5b05406>
- Fan H, Zhang M, Bhandari B, Yang C (2020) Food waste as a carbon source in carbon quantum dots technology and their applications in food safety detection. *Trends Food Sci Technol* 95:86–96. <https://doi.org/10.1016/j.tifs.2019.11.008>
- Gao G, Jiang YW, Jia HR et al (2018) On-off-on fluorescent nanosensor for Fe<sup>3+</sup> detection and cancer/normal cell differentiation via silicon-doped carbon quantum dots. *Carbon N Y* 134:232–243. <https://doi.org/10.1016/j.carbon.2018.02.063>

- Huang K, He Q, Sun R et al (2019) Preparation and application of carbon dots derived from cherry blossom flowers. *Chem Phys Lett* 731:136586. <https://doi.org/10.1016/j.cplett.2019.07.014>
- Jia J, Lin B, Gao Y et al (2019) Highly luminescent N-doped carbon dots from black soya beans for free radical scavenging, Fe<sup>3+</sup> sensing and cellular imaging. *Spectrochim Acta - Part A Mol Biomol Spectrosc* 211:363–372. <https://doi.org/10.1016/j.saa.2018.12.034>
- Kang S, Li X, Fan J, Chang J (2013) Hydrothermal conversion of lignin: a review. *Renew Sustain Energy Rev* 27:546–558. <https://doi.org/10.1016/j.rser.2013.07.013>
- Lin H, Huang J, Ding L (2019) A recyclable optical fiber sensor based on fluorescent carbon dots for the determination of ferric ion concentrations. *J Light Technol* 37:4815–4822. <https://doi.org/10.1109/JLT.2019.2922375>
- Lin C, Sun K, Zhang C et al (2020) Carbon dots embedded metal organic framework@chitosan core-shell nanoparticles for vitro dual mode imaging and pH-responsive drug delivery. *Microporous Mesoporous Mater* 293:109775. <https://doi.org/10.1016/j.micromeso.2019.109775>
- Liu W, Diao H, Chang H et al (2017) Green synthesis of carbon dots from rose-heart radish and application for Fe<sup>3+</sup> detection and cell imaging. *Sensors Actuators, B Chem* 241:190–198. <https://doi.org/10.1016/j.snb.2016.10.068>
- Liu J, Chen Y, Wang L et al (2019) Modification-free fabricating ratiometric nanoprobe based on dual-emissive carbon dots for nitrite determination in food samples. *J Agric Food Chem* 67:3826–3836. <https://doi.org/10.1021/acs.jafc.9b00024>
- Lv P, Xu Y, Liu Z et al (2020) Carbon dots doped lanthanide coordination polymers as dual-function fluorescent probe for ratio sensing Fe<sup>2+/3+</sup> and ascorbic acid. *Microchem J* 152:104255. <https://doi.org/10.1016/j.microc.2019.104255>
- Ma H, Sun C, Xue G et al (2019) Facile synthesis of fluorescent carbon dots from *Prunus cerasifera* fruits for fluorescent ink, Fe<sup>3+</sup> ion detection and cell imaging. *Spectrochim Acta Part A Mol Biomol Spectrosc* 213:281–287. <https://doi.org/10.1016/j.saa.2019.01.079>
- Nampoothiri KUK, Krishnakumar V, Thampan PK, Achuthan Nair M (2018) The coconut palm (*Cocos nucifera* L.)—research and development perspectives. Springer, Singapore. <https://doi.org/10.1007/978-981-13-2754-4>
- Nayar NM (2017) The coconut: Phylogeny, origins, and spread. Elsevier, Amsterdam. ISBN 978-0-12-809778-6
- Paksung N, Pfersich J, Arauzo PJ et al (2020) Structural effects of cellulose on hydrolysis and carbonization behavior during hydrothermal treatment. *ACS Omega* 5:12210–12223. <https://doi.org/10.1021/acsomega.0c00737>
- Sabet M, Mahdavi K (2019) Green synthesis of high photoluminescence nitrogen-doped carbon quantum dots from grass via a simple hydrothermal method for removing organic and inorganic water pollutions. *Appl Surf Sci* 463:283–291. <https://doi.org/10.1016/j.apsusc.2018.08.223>
- Sarih NM, Ciupa A, Moss S et al (2020) Furo[3,2-c]coumarin-derived Fe<sup>3+</sup> selective fluorescence sensor: synthesis, fluorescence study and application to water analysis. *Sci Rep* 10:7421. <https://doi.org/10.1038/s41598-020-63262-7>
- Standardization Administration of the People's Republic of China, The ministry of Health of the People's Republic of China (2006) Standards for drinking water quality. GB 5749-2006
- Sulaiman KS, Mat A, Arof AK (2016) Activated carbon from coconut leaves for electrical double-layer capacitor. *Ionics (Kiel)* 22:911–918. <https://doi.org/10.1007/s11581-015-1594-9>
- Sun YP, Zhou B, Lin Y et al (2006) Quantum-sized carbon dots for bright and colorful photoluminescence. *J Am Chem Soc* 128:7756–7757. <https://doi.org/10.1021/ja062677d>
- Sun D, Liu T, Wang C et al (2020) Hydrothermal synthesis of fluorescent carbon dots from gardenia fruit for sensitive on-off detection of Hg<sup>2+</sup> and cysteine. *Spectrochim Acta Part A Mol Biomol Spectrosc* 240:118598. <https://doi.org/10.1016/j.saa.2020.118598>
- Tejwan N, Saha SK, Das J (2020) Multifaceted applications of green carbon dots synthesized from renewable sources. *Adv Colloid Interface Sci* 275:102046. <https://doi.org/10.1016/j.cis.2019.102046>
- Vandarkuzhali SAA, Jeyalakshmi V, Sivaraman G et al (2017) Highly fluorescent carbon dots from Pseudo-stem of banana plant: applications as nanosensor and bio-imaging agents. *Sensors Actuators B Chem* 252:894–900. <https://doi.org/10.1016/j.snb.2017.06.088>
- Venkatesan G, Rajagopalan V, Chakravarthula SN (2019) Boswellia ovalifoliolata bark extract derived carbon dots for selective fluorescent sensing of Fe<sup>3+</sup>. *J Environ Chem Eng* 7:103013. <https://doi.org/10.1016/j.jece.2019.103013>
- Wang BB, Jin JC, Xu ZQ et al (2019a) Single-step synthesis of highly photoluminescent carbon dots for rapid detection of Hg<sup>2+</sup> with excellent sensitivity. *J Colloid Interface Sci* 551:101–110. <https://doi.org/10.1016/j.jcis.2019.04.088>
- Wang M, Wan Y, Zhang K et al (2019b) Green synthesis of carbon dots using the flowers of *Osmanthus fragrans* (Thunb.) Lour. as precursors: application in Fe<sup>3+</sup> and ascorbic acid determination and cell imaging. *Anal Bioanal Chem*. <https://doi.org/10.1007/s00216-019-01712-6>
- Wang X, Yang P, Feng Q et al (2019c) Green preparation of fluorescent carbon quantum dots from cyanobacteria for biological imaging. *Polymers (Basel)* 11:616. <https://doi.org/10.3390/polym11040616>
- Wei G, Zhao Z, Du J et al (2019) Reed-derived fluorescent carbon dots as highly selective probes for detecting Fe<sup>3+</sup> and excellent cell-imaging agents. *RSC Adv* 9:21715–21723. <https://doi.org/10.1039/c9ra01841g>
- Xu X, Ray R, Gu Y et al (2004) Electrophoretic analysis and purification of fluorescent single-walled carbon nanotube fragments. *J Am Chem Soc* 126:12736–12737. <https://doi.org/10.1021/ja040082h>
- Xu C, Zhu S, Xing C et al (2015a) Isolation and properties of cellulose nanofibrils from coconut palm petioles by different mechanical process. *PLoS ONE* 10(4):e0122123. <https://doi.org/10.1371/journal.pone.0122123>
- Xu H, Yang X, Li G et al (2015b) Green synthesis of fluorescent carbon dots for selective detection of tartrazine in food samples. *J Agric Food Chem* 63:6707–6714. <https://doi.org/10.1021/acs.jafc.5b02319>
- Xu L, Li Y, Gao S et al (2020) Preparation and properties of cyanobacteria-based carbon quantum dots/polyvinyl

- alcohol/nanocellulose composite. *Polymers (Basel)* 12:1143. <https://doi.org/10.3390/POLYM12051143>
- Yan Z, Hu L, You J (2016) Sensing materials developed and applied for bio-active  $\text{Fe}^{3+}$  recognition in water environment. *Anal Methods* 8:5738–5754. <https://doi.org/10.1039/c6ay01502f>
- Yang H, Liu Y, Guo Z et al (2019a) Hydrophobic carbon dots with blue dispersed emission and red aggregation-induced emission. *Nat Commun* 10:1789. <https://doi.org/10.1038/s41467-019-09830-6>
- Yang Y, Zou T, Wang Z et al (2019b) The fluorescent quenching mechanism of N and S Co-doped graphene quantum dots with  $\text{Fe}^{3+}$  and  $\text{Hg}^{2+}$  ions and their application as a novel fluorescent sensor. *Nanomaterials* 9:738. <https://doi.org/10.3390/nano9050738>
- Yang P, Zhu Z, Li X et al (2020a) Facile synthesis of yellow emissive carbon dots with high quantum yield and their application in construction of fluorescence-labeled shape memory nanocomposite. *J Alloys Compd* 834:154399. <https://doi.org/10.1016/j.jallcom.2020.154399>
- Yang X, Xu J, Luo N et al (2020b) N, Cl co-doped fluorescent carbon dots as nanoprobe for detection of tartrazine in beverages. *Food Chem* 310:125832. <https://doi.org/10.1016/j.foodchem.2019.125832>
- Yu J, Song N, Zhang YK et al (2015) Green preparation of carbon dots by Jinhua bergamot for sensitive and selective fluorescent detection of  $\text{Hg}^{2+}$  and  $\text{Fe}^{3+}$ . *Sensors Actuators B Chem* 214:29–35. <https://doi.org/10.1016/j.snb.2015.03.006>
- Zhang Y, Wang Y, Feng X et al (2016) Effect of reaction temperature on structure and fluorescence properties of nitrogen-doped carbon dots. *Appl Surf Sci* 387:1236–1246. <https://doi.org/10.1016/j.apsusc.2016.07.048>
- Zhang X, Jiang M, Niu N et al (2018) Natural-product-derived carbon dots: from natural products to functional materials. *Chemosuschem* 11:11–24. <https://doi.org/10.1002/cssc.201701847>
- Zhang L, Wang Y, Liu W et al (2019a) Corn cob residues as carbon quantum dots sources and their application in detection of metal ions. *Ind Crops Prod* 133:18–25. <https://doi.org/10.1016/j.indcrop.2019.03.019>
- Zhang Y, Xiao Y, Zhang Y, Wang Y (2019b) Carbon quantum dots as fluorescence turn-off-on probe for detecting  $\text{Fe}^{3+}$  and ascorbic acid. *J Nanosci Nanotechnol* 20:3340–3347. <https://doi.org/10.1166/jnn.2020.17412>
- Zhang Q, Sun Y, Liu M, Liu Y (2020) Selective detection of  $\text{Fe}^{3+}$  ions based on fluorescence MXene quantum dots via a mechanism integrating electron transfer and inner filter effect. *Nanoscale* 12:1826–1832. <https://doi.org/10.1039/c9nr08794j>
- Zhao Y, Xu C, Xing C et al (2015) Fabrication and characteristics of cellulose nanofibril films from coconut palm petiole prepared by different mechanical processing. *Ind Crops Prod* 65:96–101. <https://doi.org/10.1016/j.indcrop.2014.11.057>
- Zhao S, Song X, Chai X et al (2020) Green production of fluorescent carbon quantum dots based on pine wood and its application in the detection of  $\text{Fe}^{3+}$ . *J Clean Prod* 263:121561. <https://doi.org/10.1016/j.jclepro.2020.121561>
- Zhu S, Meng Q, Wang L et al (2013) Highly photoluminescent carbon dots for multicolor patterning, sensors, and bioimaging. *Angew Chemie Int Ed* 52:3953–3957. <https://doi.org/10.1002/anie.201300519>

**Publisher's Note** Springer Nature remains neutral with regard to jurisdictional claims in published maps and institutional affiliations.